nature communications

Article

https://doi.org/10.1038/s41467-024-54049-9

Structure-derived insights from blood factors binding to the surfaces of different adenoviruses

Received: 5 June 2024

Accepted: 30 October 2024

Published online: 11 November 2024

Check for updates

Haley E. Mudrick[1,6], Shao-Chia Lu[2,6], Janarjan Bhandari[3], Mary E. Barry[2], Jack R. Hemsath[2], Felix G. M. Andres[2,4], Olivia X. Ma[3], Michael A. Barry[2,4] ✉ & Vijay S. Reddy[3,5] ✉

The tropism of adenoviruses (Ads) is significantly influenced by the binding of various blood factors. To investigate differences in their binding, we conducted cryo-EM analysis on complexes of several human adenoviruses with human platelet factor-4 (PF4), coagulation factors FII (Prothrombin), and FX. While we observed EM densities for FII and FX bound to all the species-C adenoviruses examined, no densities were seen for PF4, even though PF4 can co-pellet with various Ads. Similar to FX, the γ-carboxyglutamic acid (Gla) domain of FII binds within the surface cavity of hexon trimers. While FII binds equally to species-C Ads: Ad5, Ad6, and Ad657, FX exhibits significantly better binding to Ad5 and Ad657 compared to Ad6. Although only the FX-Gla domain is observed at high-resolution (3.7 Å), the entire FX is visible at low-resolution bound to Ad5 in three equivalent binding modes consistent with the 3-fold symmetric hexon. Only the Gla and kringle-1 domains of FII are visible on all the species-C adenoviruses, where the rigid FII binds in an upright fashion, in contrast to the flexible and bent FX. These data suggest that differential binding of FII and FX may shield certain species-C adenoviruses differently against immune molecules, thereby modulating their tropism.

Adenoviruses (Ads) are non-enveloped icosahedral double-stranded DNA (dsDNA) viruses. Human adenoviruses (HAdVs) cause several self-limiting diseases (e.g., respiratory, keratoconjunctivitis, enteric diseases) (reviewed in refs. 1–4). HAdVs are grouped genetically into species A (HAdV-A) through G (HAdV-G) with sequence diversity at the DNA level being as high as 40%[5]. This genetic diversity translates into variations in genome activation in different cell types and requires varied strategies to combat the immune system surveillance and clearance. Many of these variations are also manifested on the protein surface of the virion particularly in major capsid proteins - hexon, fiber, and penton base (PB). Variations in the trimeric fiber protein translate into differences in its length, flexibility, and in their ability to bind to different receptors for cell entry (i.e. coxsackie and adenovirus receptor (CAR), CD46, desmoglein-2, α-V integrins, etc.)[4]. This genetic diversity is particularly reflected in the hypervariable regions (HVRs) of the hexon protein that makes up the bulk of the virion surface. The sequence diversity in HVRs is driven by evolution to evade neutralizing antibodies against different Ad serotypes[6,7]. The 720 hexons present in each Ad virion, arranged as 240 trimers, from a highly patterned icosahedral capsid surface for the host proteins to bind to and fundamentally change the tropism of the virus and its detection by and activation of the innate and adaptive immune system[8–17].

[1]Molecular Pharmacology and Experimental Therapeutics Graduate Program, Mayo Clinic, Rochester, MN 55905, USA. [2]Department of Internal Medicine, Division of Infectious Diseases, Mayo Clinic, Rochester, MN 55905, USA. [3]The Hormel Institute, University of Minnesota, Austin, MN 55912, USA. [4]Department of Immunology, Department of Molecular Medicine, Mayo Clinic, Rochester, MN 55905, USA. [5]Department of Integrative Structural and Computational Biology, Scripps Research, La Jolla, CA 92037, USA. [6]These authors contributed equally: Haley E. Mudrick, Shao-Chia Lu. ✉e-mail: mab@mayo.edu; vsreddy@umn.edu

The host protein interactions with the hexon surface may play a major role during virus natural lifecycle and the resulting immune responses if Ads breakout from their usual mucosal site of infection and leak into the bloodstream[11]. However, these interactions are most important when considering the use of Ad vectors in molecular therapies while delivering by intravenous (IV) injection. They may also contribute to side effects like vaccine-induced thrombocytopenia (VITT) if Ads leak into the bloodstream due to muscle tissue damage after needle injections[18–22].

Binding or lack of binding of blood factors to various Ad serotypes strongly influences their ultimate pharmacological fate in vivo. Ads have a half-life of less than 2 min in the bloodstream after IV injections in mice[23,24]. Much of IV injected virus is sequestered and destroyed by cells of the reticuloendothelial system (RES). In the liver, Kupffer cell macrophages are a large trap for incoming Ads[12,13,15,16]. Destruction of different Ad serotypes by Kupffer cells and the RES is modulated positively or negatively by the binding of host blood proteins to the virion surface[10,12,13,15,16]. Natural and adaptive antibodies can bind Ad virions and target them for complement deposition and/or agglutination followed by phagocytosis and destruction[17,25].

Certain Ad serotypes are shielded to varying degrees by the binding of γ-carboxyglutamic acid (Gla) domains of vitamin K-dependent blood clotting factors including FII (prothrombin), FVII, FVIII, and FX to hexons on the AdV surface[8,13,26,27]. These factors do not bind to most Ad serotypes with high affinity[10], however, in contrast, they bind to species-C human Ads with high, but variable affinities[8,10,17]. Thus, species-C Ads may have a special ability to evade complement deposition and their destruction by Kupffer cells when compared to other Ads that do not bind these vitamin K-dependent blood clotting factors.

Even within species-C Ads, there is variation in the tropism and destruction of different serotypes. When species-C Ad1, Ad2, Ad5, and Ad6 were compared by IV injection in BALB/c mice having higher concentrations of natural antibodies, Ad6 followed by Ad5 mediated the strongest liver transduction[5]. This function appears to be intrinsic to the Ad6 hexon as demonstrated by the enhanced ability of transduction due to the modified Ad5 by exchanging its hexon HVRs with those of Ad6[28]. This higher activity correlated with reduced phagocytosis by macrophages and decreased binding by scavenger receptors[28]. While it is still somewhat unclear why Ad6 performs better, some of these effects are highly dependent on the levels of IgM natural antibodies in different mouse strains and likely in humans[15]. Recent seminal work provided insights into differences in the functionality of species-C Ads by revealing that they bind FII and FX with quite different affinities[17].

Beyond vitamin K-dependent blood factors, it was suggested that platelet factor 4 (PF4) also binds to many Ads[22] and may be involved in causing the VITT side effect after intramuscular vaccination with the Ad-vectored COVID-19 vaccines[18–22]. It has been reported that PF4 appears to bind to Ad5, Ad26 and ChAdOX1 with affinities of 0.789, 0.661, and 0.301 μM, respectively[22], which are approximately 1000-fold lower than the affinity with which FX binds to Ad5 (0.74 nM)[17]. Moreover, the median concentration of PF4 in human blood is 7 ng/ml[29], compared to 1000-fold higher concentration of FX at 8 μg/ml[10]. Notably, FII's concentration in plasma is 117 μg/ml[30] making it about 15 times higher than FX and 10,000 times higher than PF4. These data show that a variety of blood factors bind to the surfaces of several Ad serotypes and modulate their tropism, by affecting their ability to interact differently with the immune molecules. The data also show that there are strong differences in the ability of different Ads to bind to the blood factors. Previous structural studies primarily focused on FX interacting with Ad5[8,10,11] and another study involved FVIII binding also to Ad5[31].

In this work we performed biochemical and structural studies to better understand the characteristics of the multiple blood factors - PF4, FII, and FX binding to human species D Ad26 and three species-C Ads: Ad5, Ad6, and Ad657. The Ad657 vector that we used in this study is a modified Ad6 vector, termed Ad657, where the Ad6 hexon-HVR sequences were replaced by the corresponding Ad57 sequences[32]. The results from the cryo-EM studies highlight the locations, structural characteristics and interactions between the blood factors and different Ads and their potential implications to vector transduction properties and immune clearance.

Results

Biochemical analysis of FX, FII, and PF4 binding to Ads

It has been shown that PF4 can bind to hexons of many Ads with low affinities (300 to 790 nM)[22], but at much (1000-fold) lower affinities compared to other blood factors (e.g., FX, 0.74 nM) binding to hexons[17]. Given the concerns that PF4 binding to Ads may have a role in the clotting disorders observed with Ad COVID-19 vaccines[18–22], we performed biochemical and cryo-EM studies to examine this interaction. The median concentration of PF4 in human blood is rather low at 7 ng/ml[29] compared to 1000-fold higher concentration of FX at ~7 μg/ml[10] and 14,000-fold higher concentration of FII (100 μg/ml)[30] Given this, we mixed these proteins at their physiological concentrations found in the blood with species-C Ad5 and Ad6, Ad657, and species D Ad26 and performed pull-down assays. Under these conditions, both FX and FII co-pelleted with the species-C viruses (Ad5, Ad6, and Ad657) as detected by western blot analysis and interestingly both the proteins co-precipitated weakly with Ad26 (Supplementary Figs. 1a and 1b). While the FX and FII binding could be detected in a serotype-specific fashion, PF4 was not detectable by western blot when using physiological concentration of PF4 for complex formation (Supplementary Fig. 1c). Given this, PF4 was incubated with the viruses at a 1000-fold higher than normal concentrations of 7 μg/ml. Under these super-physiological conditions, the 7.8 kDa PF4 monomer appears to co-pellet with all of the viruses (Supplementary Fig. 1d).

Cryo-EM analysis of PF4 binding to HAdVs

We collected cryo-EM data and obtained canonical icosahedral 3D-reconstructions of the samples of Ad5, Ad6 and Ad657 incubated with PF4 but failed to observe significant densities corresponding to PF4 even when the super-physiological concentrations of the factor were used (Supplementary Fig. 2). Of note, even though the difference densities that belong to the disordered HVR1 regions could be seen, as in the case of native Ads, we did not observe any densities that can be attributed to PF4. The absence of PF4 densities in the 3D-reconstructions of the complexes is consistent with the low affinities of PF4 binding to various and/or lack of specific binding as observed by the biochemical analysis.

Cryo-EM analysis of Ad5-FX complex

We resolved the icosahedrally averaged structure of Ad5-FX complex at 3.61 Å resolution (Fig. 1, Supplementary Table 1). In agreement with the previous observations that human FX binds strongly to Ad5 over Ad657 and Ad6[17], we see strong densities of FX bound to Ad5 hexon (Fig. 1, Supplementary Fig. 3). While we mainly observed strong densities for the Gla domain in hexon cavities at high resolution (3.6 Å), the densities for epidermal growth factor-like (EGF) and serine protease (SP) domains are evident in low-resolution maps (~10 Å) (Fig. 1, Supplementary Fig. 3). This is likely because of the apparent flexibility of FX causing in disorder at high resolution. It is notable that although we see FX adopting three possible binding modes consistent with the 3-fold symmetry of hexon, only one of those modes of binding is possible at any given time (Fig. 1C-F). The simultaneous visualization of 3 binding modes in all the 4 unique hexons of Ad5-FX complex (Supplementary Fig. 3) is an artifact of icosahedral symmetry averaging of the dataset containing 1000 s of particles, wherein FX can bind to each hexon in a particle in any one of 3 different ways that are sterically allowed.

In an attempt to capture a single FX binding mode, we obtained a localized reconstruction of one of the unique hexons (hexon-4) in C1

https://doi.org/10.1038/s41467-024-54049-9

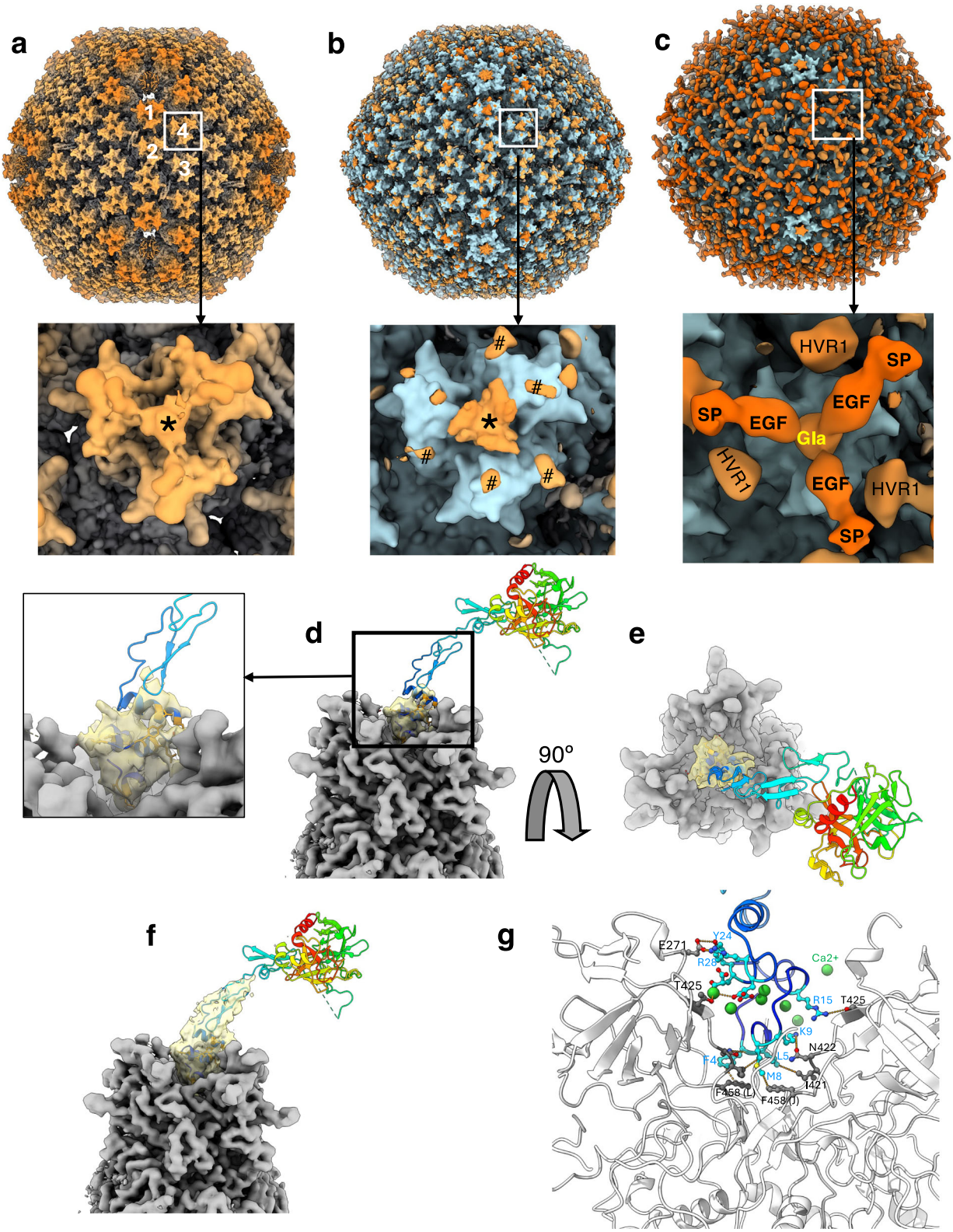

symmetry followed by relaxation of the C3 symmetry of the hexon[33,34]. Even though we could not completely resolve the C3-symmetry into 3 equivalent binding modes, we could unambiguously select one of the 3 binding modes (Fig. 1f; Supplementary Fig. 3). Docking the AlphaFold2 generated model[35] of FX into the corresponding densities of the localized reconstructions (Supplementary Fig. 4) using ChimeraX[36,37], followed by real space (RS) refinement using Phenix[38,39] and further model adjustments in Coot[40,41], revealed the interactions between the Gla domain of FX and Ad5 hexon (Supplementary Table 2). In addition to some of the previously identified residues, 420-426 in HVR7 of Ad5-hexon[10,11,17], we also observed that E271 in HVR5 of three hexon subunits interact with multiple residues in the Gla domain. Significantly, F4 of the Gla-domain sits on top of three F458 residues from the hexon subunits and is involved in stacking interactions (Fig. 1g). Remarkably, the corresponding phenylalanine (F) residues in the species-C AdV hexons are conserved as well as in the Gla domains of coagulation

Fig. 1 | Cryo-EM reconstruction of Ad5-FX complex and hexon-FX interactions. **a** Icosahedral reconstruction of Ad5-FX at 3.6 Å, a radially color-coded representation, displayed on a binned by 2 grid (contour level: 0.006). Unique hexons are numbered 1–4. It is notable that the PBs and fibers are weakly ordered. Shown below is a zoomed-in view of the hexon-4. The location of the FX-Gla-domain density found in the hexon cavity is identified by an asterisk. **b** A difference map at 3.6 Å, calculated by subtracting the Ad5 atomic model map (blue) from the Ad5-FX map shown in (**a**). The zoomed-in view below identifies the densities that belong to FX, identified by an asterisk and those that belong to the missing hexon-HVR loops are identified with the symbol "#". **c** A difference map at 10 Å showing the blobs of FX density corresponding to 3 modes of FX binding to a single hexon (contour level: 0.0002). Zoomed-in view below identifies the locations of different domains of FX (Gla, EGF1&2, SP) and missing HVR1 loops. Of note, even though it appears that 3 copies of FX are bound to a single hexon, only a single copy of FX can bind to one hexon as the hexon cavity can accommodate a single Gla domain (Supplementary Fig. 3). **d** A localized reconstruction of hexon-FX complex at ~3.6 Å resolution. A modified AlphaFold2 model of FX containing Gla residues (rainbow ribbon) is docked into the corresponding density (khaki) for the Gla domain (contour level: 0.025). Shown on the left is a zoomed-in diagram of the boxed region. **e** A 90° rotated view of (**d**). **f** A localized reconstruction of hexon-FX (as in **b**) showing the density for EGF domain (khaki) displayed at a lower contour level (contour level: 0.0025). **g** Interactions between the Gla domain (blue) and the hexon trimer (gray). The interacting residues, FX-Gla (cyan) and hexon (gray), are shown in ball-and-stick representation with the dotted lines indicating some of the pairs of interacting residues. Ca^{2+} ions are shown as green spheres. The details of these interactions are listed In Supplementary Table 2.

factors, II, VII and X with exception of Factor-IX. The "greasy" interaction involving the aromatic (Phe) residues may allow the free rotation of the Gla domain in the hexon cavity. Figure 1g shows the Ad5-hexon residues that interact with the Gla domain of FX. Moreover, a critical HVR7 residue of Ad5:hexon, Thr425, has been shown to be important for FX binding[11,17] is involved in the Ca2+ mediated interactions with Gla residues (Supplementary Table 2). In addition to allowing FX to bind to Ad5-hexons in multiple (3) modes, having a wider entrance to the hexon cavity (Supplementary Fig. 14) may result in higher affinities of association between FX and Ad5 (hexon) compared to other species-C Ads.

Cryo-EM analysis of Ad657-FX complex

We determined the icosahedrally averaged structure of Ad657-FX complex at 4.0 Å resolution. Interestingly, unlike the Ad5-FX complex, we did not see strong evidence for the 3 equivalent modes of FX binding to Ad657 hexons in icosahedrally averaged maps even at low resolution (Supplementary Fig. 5). Even though we observed only a single mode of FX binding to Ad657 hexons in the icosahedral and localized reconstructions (Fig. 2c, Supplementary Fig. 16), it is still possible that FX could bind to Ad657-hexon in multiple binding modes, but not as easily as to Ad5-hexon. Calculating the contacts between the Gla domain of FX and Ad657 hexon suggest that in addition to interactions with the HVR7 residues (G427, V428 and T431), multiple residues (277-282) from HVR5 are involved in contacting the Gla domain (Supplementary Table 2). Of note, the HVR5's are located at the entrance/rim of the hexon cavity, wherein the Gla domain binds (Fig. 2 a, b). We hypothesize that the greater number of interactions observed between the Ad657-HVR5 residues and the FX-Gla domain are likely to restrict the FX binding to Ad657 hexons to specific (fewer) ways. This is in contrast to Ad5-FX complex, where the multiple modes of FX binding to Ad5-hexon and fewer interactions with the HVR5s and wider entrance to the cavity are observed. Taken together, modifications to HVR5 could potentially influence the FX binding in agreement with the experimental observations by Benihoud and colleagues[9].

Cryo-EM analysis of Ad6-FX complex

Even though we were not successful in obtaining Ad6-FX in our first attempt, we observed the density for FX bound to Ad6 in our second attempt by increasing the amount of FX used (Supplementary Table 2, Supplementary Fig. 6). This is likely due to ~40x lower affinity of FX binding to Ad6 than to Ad5[17]. While the conventional icosahedral 3D-reconstruction yielded a 5 Å resolution map, the localized reconstruction of Hexon(4)-FX sub-volume improved the resolution to 4.3 Å (Supplementary Table 1, Supplementary Table 4). This allowed us to dock the FX model into the corresponding density and obtain the interactions between the FX and Ad6-hexon (Supplementary Table 2, Fig. 2d). Of note, in addition to total number of interactions between the hexons and factors, the kinetics of binding (i.e., on and off-rates) could influence the relative binding affinities of factors binding to various Ads.

The superposition of hexon structures from the unbound and bound Ad6-factor complex reconstructions revealed conformational changes in HVR5 loops opening of the entrance to the cavity (Supplementary Fig. 7). But it is notable that Ad6 hexon displays a narrow entrance to the hexon cavity relative to the hexons of Ad5 and Ad657 (Supplementary Fig. 14). The extent of opening of entrance to the hexon cavity may play a role in influencing the on and off-rates of FX binding to Ad6 and other Ads in general, thereby impacting their relative binding affinities.

Cryo-EM analysis of Ad5-FII complex

We determined the icosahedrally averaged structure of Ad5-FII complex at 4.13 Å resolution. The Gla domain of FII is larger than that of FX by 15 amino acids. Despite this, it binds similarly to FX in the Ad5 hexon cavity (Fig. 3). While we were able to observe clear densities for both the Gla and kringle-1 (KR1) domains of FII, they could not be resolved to the same extent as the hexon densities. This could be due to our inability resolve multiple modes of binding and/or flexibility of bound factors. However, we were able to dock the AlphaFold2-generated model of FII into the corresponding densities (Fig. 3b). It appears that the rigid and stubby nature of FII structure enables it to bind to Ad5 in an upright fashion in the hexon cavity compared to the more flexible and bent FX molecule (Fig. 3c). Superposition of Ad5:hexon-FX complex onto Ad5:hexon-FII complex derived from the localized reconstructions suggest that FX binds deeper into the hexon cavity relative to FII. In support of this, we observe fewer residues of the Gla domain of FII interact with Ad5-hexon compared to FX-Gla domain in Ad5-FX complex (Supplementary Tables S2 and S3). This is also in agreement with the binding affinities determined by SPR, where FII appears to bind Ad5 hexon nearly 50x weaker than FX[17]. Although it is possible that FII, like FX, also could bind to Ad5 hexon in three equivalent binding modes, we did not see clear evidence supporting such a scenario. However, it may be still possible that the Gla domain of FII can freely rotate in the hexon cavity aided by hydrophobic interactions (greasy patch) of phenylalanine F4 of the Gla domain with three F458 phenylalanine residues contributed by each hexon monomer.

Cryo-EM analysis of Ad6-FII complex

Among the structures of Ad-FII complexes, the Ad6-FII complex yielded the highest resolution structure at 3.7 Å, consistent with the highest affinity of interactions observed between Ad6 and FII[17]. As in the Ad5-FII structure, there are clear densities seen for both the Gla and KR1 domains, while the remaining KR2 and SP domains are disordered (Fig. 4). Superposition of Ad5 (hexon)-FII structure on to Ad6 (hexon)-FII structure suggests that FII binds deeply in the Ad6 hexon cavity compared to Ad5 hexon (Supplementary Fig. 10). Furthermore, we observe that twice as many residues in the FII-Gla domain interact with Ad6 hexon compared to Ad5 hexon (Supplementary Table 3) which is consistent with the higher affinity interaction between Ad6 hexon and FII (K_D = 2.7 nM) compared to the interaction between Ad5 hexon and FII (K_D = 39 nM)[17]. Again, we observe the conserved "greasy" interaction

https://doi.org/10.1038/s41467-024-54049-9

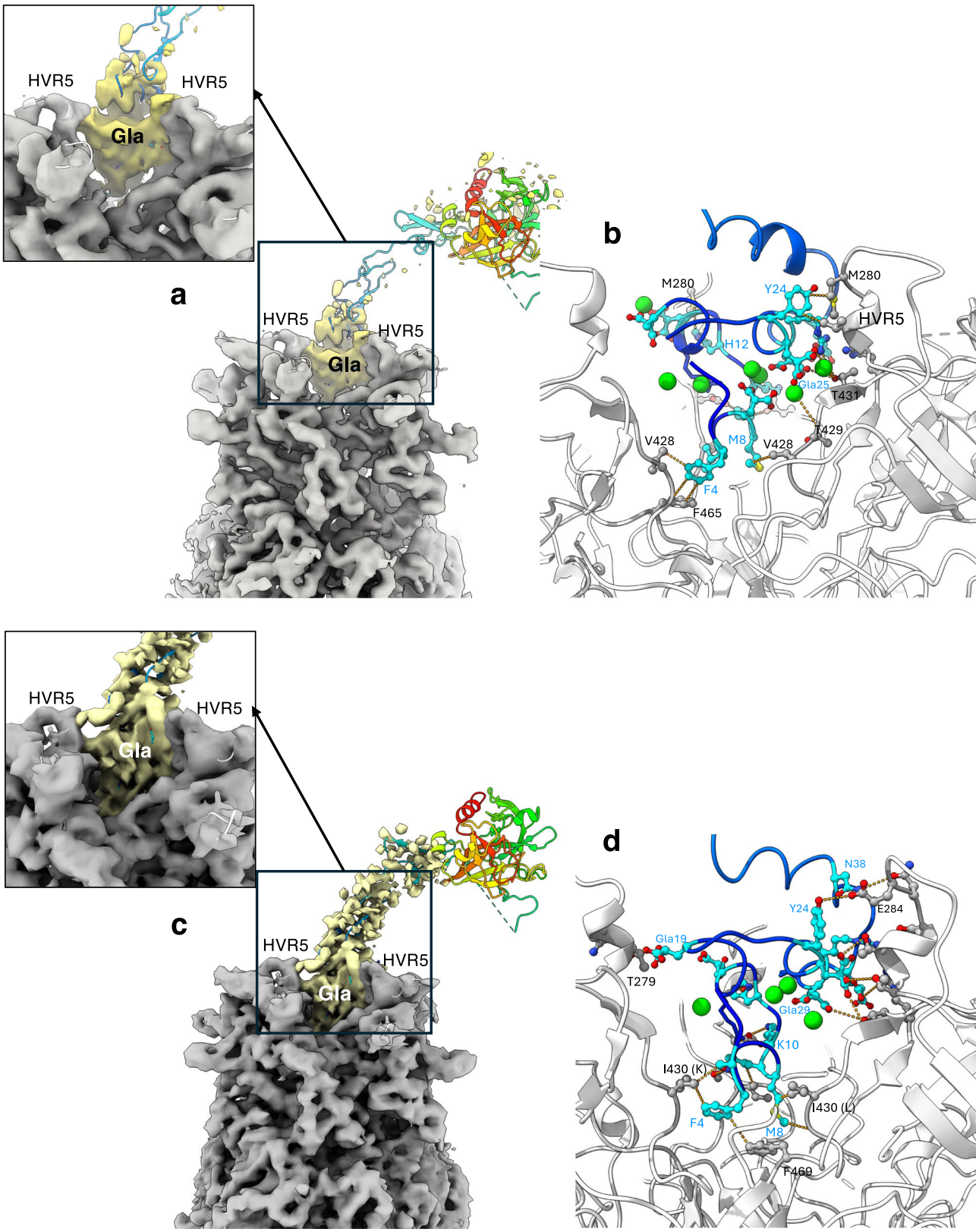

between F4 of the Gla domain and F469 residues from the Ad6 hexon subunits that allows the free movement of the Gla domain in the hexon cavity.

Cryo-EM analysis of Ad657-FII complex

The modest resolution (~4 Å) structure of Ad657 (hexon)-FII complex allowed us unequivocally to fit the hexon Ad657 sequence and dock the Gla and KR1 domains of the AlphaFold2 model of FII into the EM-densities (Fig. 5). Calculation of the interactions (contacts) between the FII-Gla domain and Ad657-hexon suggests similar number of Gla domain residues are involved as observed in the case of Ad6-FII (Supplementary Table 3). This in turn suggests that FII binds to Ad657 and Ad6 hexons with comparable affinities, both significantly better than binding to Ad5-hexon.

Fig. 2 | Hexon-FX interactions in Ad657-FX and Ad6-FX complexes. a Localized reconstruction of Ad657:hexon-FX complex at 3.86 Å (contour level: 0.014) derived from the icosahedral reconstruction of the Ad657-FX complex illustrated in Supplementary Fig. 5. The inset shows a zoomed-in view of the FX-Gla domain docked into the corresponding density shown in yellow. Location of HVR5 loops and the Gla domain are identified. **b** A closeup view of Ad657-hexon and FX interactions. Hexon model near the Gla-domain binding cavity is shown as gray ribbons. The interacting hexon and FX-Gla residues are shown in ball-and-stick representation, in gray and cyan colors, respectively and the Ca^{2+} are shown as green spheres. Some of the interacting residues are connected with dotted lines. Further details of the interacting residues are provided in Supplementary Table 2. **c** Localized reconstruction of Ad6:hexon-FX complex at 4.3 Å (contour level: 0.01) derived from the icosahedral reconstruction of the Ad6-FX complex illustrated in Supplementary Fig. 6. The inset shows a zoomed-in view of the FX-Gla domain docked into the corresponding density shown in yellow. **d** A closeup view of Ad6-hexon and FX interactions. Hexon model near the Gla-domain binding cavity is shown as gray ribbons. The interacting hexon and FX-Gla residues are shown in ball-and-stick representation, in gray and cyan colors, respectively and the Ca^{2+} ions are shown as green spheres. Some of the interacting residues are connected with dotted lines. Further details of the interacting residues in Ad-FX complexes are listed in Supplementary Table 2.

Discussion

We successfully obtained multiple species-C adenovirus complexes with coagulation factors FX and FII and determined their cryo-EM structures at near atomic resolution (Supplementary Table 1). There is clear evidence that the Gla domains of these factors bind in the hexon cavities lined with the residues from HVR5 and HVR7 (Figs. 1–5). We observe EM-densities for the Gla domains of both the factors and EGF1 and KR1 domains of FX and FII, respectively albeit at low resolution, however, the rest of the factor molecules (EGF2, KR2, SP domains) are disordered. While the majority of the hexon regions are well resolved to near atomic resolution (Supplementary Fig. 12), the EM-densities for the Gla domain are sufficiently resolved to fit the secondary structural elements (i.e., helices), but not good enough to model the corresponding amino acid sequence. The weak densities observed for the factors even in the localized reconstructions are likely due to our inability to resolve multiple modes of factors binding to hexons. Hence, we obtained the AlphaFold2 generated models for FX and FII molecules and docked them into respective densities. Additionally, the multiple modes of FX binding to Ad5-hexon may result in higher affinity of FX binding to Ad5 over other species-C adenoviruses and wider entrance to the hexon cavity (Supplementary Fig. 14). The Ca^{2+} mediated interactions involving Thr425 of Ad5:hexon and Gla residues in FX and FII (Supplementary Tables S2, S3) supports its role as a critical residue in binding to FX in agreement with experimental observations[17].

In addition to previously identified residues in the HVR7 region of hexons (e.g., 421–425 of Ad5) that interact with the Gla domains[10,11], we observed a few residues from HVR5 contacting the Gla domain, particularly prominent in Ad6 and Ad657 hexons (Supplementary Tables 2 and 3). These findings agree with the mutational studies involving the residues in HVR5 (e.g., E271) that influence FX binding to Ad5[9,42]. Since HVR5 is located at the entrance (mouth) of the hexon cavity, it could potentially restrict the ways the factors enter/bind in the cavity. This particularly appears to be true in the case Ad6, where the span of the entrance to the cavity estimated by the distances between HVR5 loops is narrower (~31.5 Å) compared to Ad657 and Ad5 (34-38.5 Å) (Supplementary Fig. 14). This makes Ad6 more restrictive and/or selective in binding to factors in comparison to Ad5 and Ad657, even though there is only one residue difference between Ad6 and Ad657 in this region (Ad6 I430V). Additionally, having a larger entrance to the cavity as in the Ad5 hexon allows the rapid capture (faster on-rate) of FX molecules (which have a smaller Gla domain) into the cavity, akin to having a larger size baseball glove. Once the factor is captured it is difficult for it escape the pocket (slower off-rate)[17]. Having a wider binding cavity may also result in 3 modes of binding seen in Ad5-FX complex. Smaller entrance to the cavity may restrict easy access of binding pocket by the factors and it takes longer to properly position in the cavity (slower on-rate). If the factors are not positioned correctly, they can be easily washed away (faster off-rate). Based on these findings, we hypothesize that FX binds to Ad6 weaker than Ad657 and Ad5, with relative binding affinities - K_D values - Ad6 > Ad657 > Ad5.

Moreover, a cluster of aromatic (Phenylalanine) residues, 3 from hexons and one from Gla domain of the factors, form a greasy patch at the bottom of the hexon cavity that may allow the free rotation of Gla domain within the hexon cavity similar to "ball-and-socket" joint. This in turn allows the movement of bound factors in the hexon cavity and thereby resulting in better shielding of Ad surfaces (Fig. 6). Even though, we did not observe significant conformational changes in the factors (FX/FII) upon binding to Ads, the variance in their inherent flexibility (Supplementary Fig. 13) – bent vs. upright arrangement while binding - thereby affecting their reach. This along with the differences in the Coulombic surface charge potential and the size – 240 a.a. (FX) and 330 a.a. (FII) - of their SP domains (Supplementary Fig. 15) may play a role in their transduction efficiencies of the target cells[17].

Methods

Biochemical analysis of factors binding to Ads

Ad5, Ad6, Ad657, and Ad26 were grown in 293 cells (Microbix, Toronto, Canada) and purified by double CsCl banding[43,44]. Briefly, each Ad was scaled up and propagated into a 10-layer CellSTACK chamber (Corning, Corning, NY). The collected cell pellets were resuspended in 7 mL of 20 mM HEPES buffer (pH 7.4) and lysed using 2 mL of 5% sodium deoxycholate for 30 min at room temperature. The lysates were then treated with 150 μL of DNase I (10 mg/mL) (Sigma-Aldrich, St. Louis, MO), 15 μL of PureLink™ RNase A (10 mg/mL) (Thermo Fisher Scientific, Carlsbad, CA), and 170 μL of 2 M $MgCl_2$, followed by incubation for an additional 30 min at 37 °C. After centrifugation at 3000 × *g* for 15 min at 4 °C, the resulting supernatant underwent two sequential CsCl gradient ultracentrifugation steps at 26,000 × *g*. The purified virus particles (vp) were desalted using PD-10 desalting columns (Cytiva, Marlborough, MA) in sucrose buffer (0.5 M sucrose, 20 mM HEPES). The concentration of vp per mL was estimated by measuring the OD260 with a NanoDrop Microvolume Spectrophotometer (Thermo Fisher Scientific, Carlsbad, CA). Ad657 is a chimera of Ad6 in which all of its hexon HVRs have been replaced by those from Ad57[32,45].

A total of ~4×10^{10} purified vp of Ad5, Ad6, or Ad26 were incubated overnight at 4 °C with normal blood physiological concentrations of human FX (7 μg/ml, Prolytix Inc.), or human FII (100 μg/ml, Prolytix, Inc.) or human PF4 (7 ng/ml, Chromatech Inc.) in phosphate-buffered saline pH 7.4 with Ca^{2+} Mg^{2+} (PBS (+/+), Invitrogen) containing physiological concentrations of human serum albumin (HSA, 40 mg/ml, SeraCare Lifescience, Inc.). Because PF4 could not be detected bound to any of the Ads tested at above (natural) concentrations, viruses were also incubated with super-physiological concentrations of PF4 (7 μg/ml). Virus complexes were pelleted by centrifugation in a microfuge at 21,000 × *g* for 30 min at 4 °C. Supernatants were removed and the pellets were resuspended in 300 μL PBS (+/+) and centrifuged again at 21,000 × *g* for 30 min at 4 °C. The supernatants were removed, and pellets were resuspended in 20 μL PBS (+/+) and 5 μL of 5X SDS-PAGE loading buffer with + 5 mM dithiothreitol and were heated at 95 °C for 5 min prior to their separation on TGX 4–20% gradient SDS-PAGE gels (BioRad, Inc). Proteins were transferred to a PVDF membrane, blocked with 5% skim milk in 1× Tris-Buffered Saline containing 0.1% Tween (TBST), and immunoblotting was performed with a polyclonal goat anti-human FX antibody (1:1000, AF1063, R&D Systems,

https://doi.org/10.1038/s41467-024-54049-9

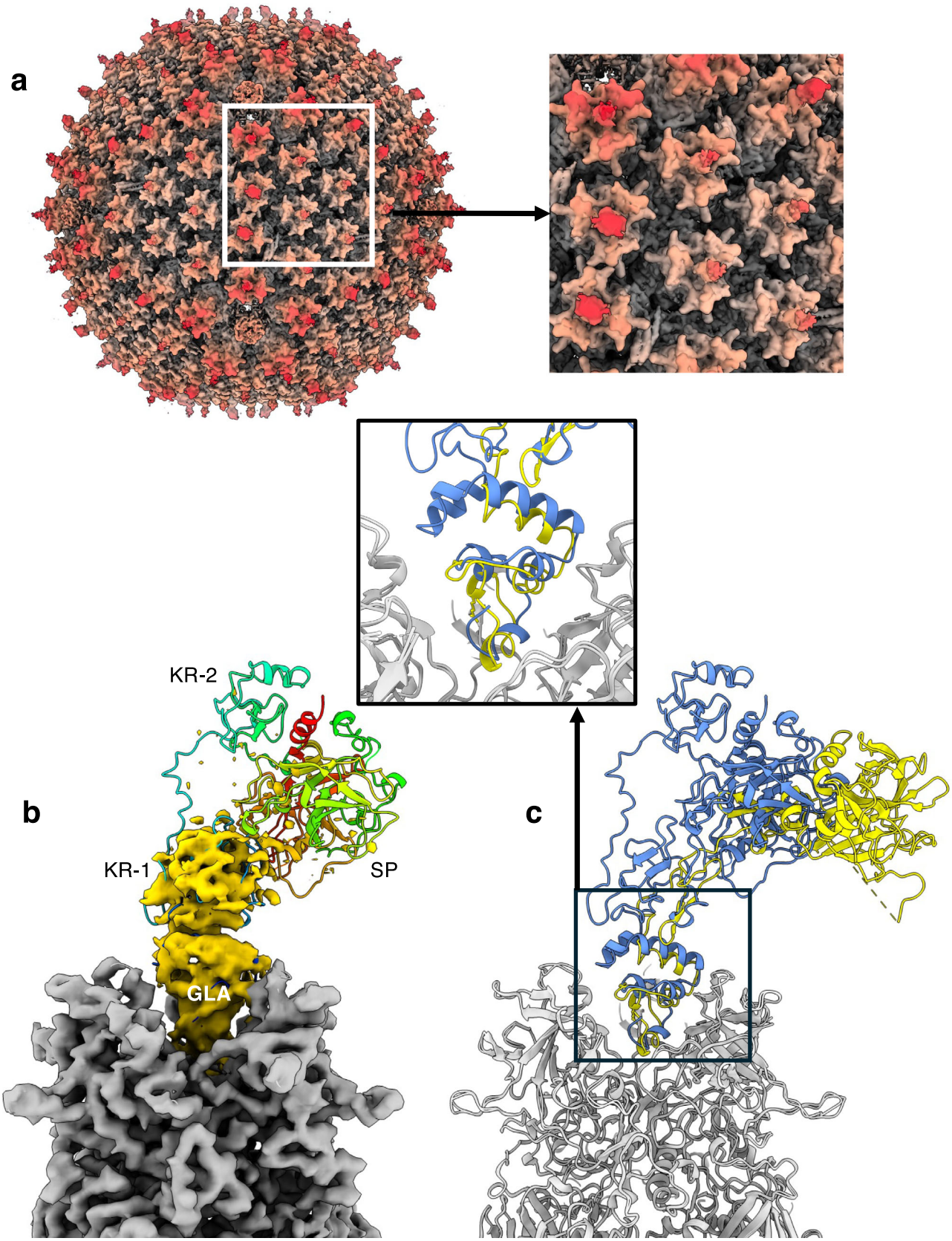

Inc.), a polyclonal rabbit anti-human FII antibody (1:1000, PA5-77976, ThermoFisher Scientific) and a monoclonal mouse antibody against human PF4 (1:100, sc-374195, Santa Cruz Biotechnology). Primary antibodies were detected with species-matched HRP-conjugated rabbit anti-goat IgG (H + L) secondary antibody (1:10000, #31402, ThermoFisher Scientific), donkey anti-rabbit IgG (H + L) cross-adsorbed secondary antibody (1:10000, # 31458, ThermoFisher Scientific) or goat anti-mouse IgG (H + L) secondary antibody (1:10000,

Fig. 3 | Cryo-EM reconstruction of Ad5-FII complex and hexon-FII interactions. **a** Icosahedral construction of Ad5-FII at 4.1 Å. A radially color-coded representation with the bright red regions at the highest elevation corresponds to the bound FII molecules (contour level: 0.009). Inset shows a zoomed-in view of the white-boxed region. Of note, the PBs and fibers are weakly ordered/disordered. **b** A localized reconstruction of hexon-FII complex (contour levels: 0.02 (hexon), 0.007 (FII)). A modified AlphaFold2 model of FII with Gla residues is docked into the corresponding density shown in yellow. While the densities corresponding to the Gla and KR1 domains can be seen, the densities corresponding to KR2, and SP domains are disordered. **c** Superposition of Ad5-FII and Ad5-FX complexes. Hexon molecules are shown in gray, while the FII and FX molecules are shown in blue and yellow, respectively. The inset shows the zoomed-in view of the boxed area, where the FX-Gla domain appears to bind deeper than that of FII-Gla domain. Further details of the interacting residues in Ad-FII complexes are listed in Supplementary Table 3.

#31430, ThermoFisher Scientific), followed by development with Super Signal West Pico (Thermofisher) on a Bio-Rad Chemidoc imaging system.

Generation of Ad-PF4 complexes for cryo-EM

Ad-PF4 complexes were generated by mixing the factors (PF4, Chromatech Inc.) with respective Ads in V-Buffer (50 mM HEPES pH 7.2, 300 mM NaCl, 10 mM CaCl2 and 5 mM MgCl2) as described above. The concentrations of the Ads and PF4 used are given in Supplementary Table 5. Ad-PF4 mixtures were incubated on a rocker overnight at 4 °C and subsequently pelleted by centrifugation at 21,000 × *g* for 30 min at 4 °C. The supernatant was removed, the pellet was resuspended for 5–6 h. in the V-buffer and adjusted to a final concentration of ~2 mg/ml of the virus-factor complex and used for preparing the cryo-EM grids.

Generation of Ad-coagulation factor complexes for cryo-EM

Ad-factor complexes were generated by mixing the factors (FX or FII, Prolytix Inc.) with respective Ads in V-Buffer (50 mM HEPES pH 7.2, 300 mM NaCl, 10 mM $CaCl_2$ and 5 mM $MgCl_2$) at hexon trimer to factor stoichiometric ratios of 1:2 and then diluting them in 1 ml of PBS (+/+). The details of concentration of virus and factors used in this study are given Supplementary Table 5. The number of hexon trimers were considered as 240 per Ad particle. The mixtures were incubated on a rocker overnight at 4 °C and subsequently pelleted by centrifugation at 21,000 × *g* for 30 min at 4 °C. The supernatant was removed, the pellet was resuspended in the V-buffer and adjusted to a final concentration of ~2 mg/ml of the virus-factor complex and used for preparing the cryo-EM grids. Of note, the elapsed time from the start of resuspending the Ad-factor pellets in V-buffer to vitrification of samples ranged between 12–15 h.

Cryo-EM sample preparation and data collection

Three microliters of Ad-factor complexes were applied twice (blotting in between) to glow-discharged grids (Quantifoil R1.2/1.3, Cu 300) and vitrified by plunge-freezing into liquid ethane using a vitrification apparatus (Vitrobot Mark IV; Thermo Fisher Scientific). Data were acquired using a 300-kV transmission electron microscope (Titan Krios; Thermo Fisher Scientific) equipped with a Gatan K3 direct electron detector attached to a BioContinuum imaging filter (slit width: 20 eV). Movies comprising 40 frames were collected at a dose rate of about 20 e-/px/s (total dose of ~80 e-/Å^2) at a calibrated magnification of ×81,000, and a pixel size of 1.1 Å. Data were collected using Thermo Scientific EPU software. Data acquisition statistics are summarized in Supplementary Table 1.

Data processing and structure determination

Movie frames were aligned using MotionCor2[46] to correct for stage drift and beam-induced motion. The resulting motion-corrected micrographs were used for subsequent data processing and analysis. The contrast transfer function (CTF) and defocus parameters were estimated using CTFFIND4[47]. The particles were automatically picked using a template derived from 1000 manually picked particles in RELION-4.0[48]. Extracted particles in a box size of 1024 pixels^2 (pixel size = 1.1 Å) were binned by 4 (pixel size = 4.4 Å) and subjected to reference-free 2D-classification. The promising 2D classes exhibiting icosahedral particle features were selected and subjected to 3D classifcation using one of the human adenovirus maps solved in our lab as a reference map with a particle diameter of 1100 Å in C1 symmetry. Again, the promising 3D classes were combined and subjected to 3D auto-refinement with icosahedral (I1) symmetry in RELION-4.0, followed by extracting particles in a rescaled box size of 800 pixels^2 with a resampled pixel size of 1.408 Å. We chose to work with this box size knowing that we may not achieve a resolution better than 2.8 Å (Nyquist limit) and to reduce the computer memory requirements and to speed up the calculations. These rescaled particles were subjected to 3D auto-refinement imposing icosahedral (I1) symmetry, followed by a round of post-processing, CTF refinement, another round of 3D auto-refinement with icosahedral symmetry with a finer angular sampling (–offset_range 3.0 –offset_step 1.0 –sigma_ang 2.0) and finally post-processing and map sharpening using a B-factor of −100Å^2. The details of data statistics and the results of structure determination are given in Supplementary Table 1. A representative workflow of the single particle analysis (SPA) procedures described above is shown in Supplementary Fig. 17. Fourier shell correlation (FSC) plots, local resolution maps and angular distribution of particles for various icosahedral and localized reconstructions of Ad-FX and Ad-FII complexes are shown in Supplementary Figs. 18–23.

Model building

The B-factor sharpened maps were imported into the structure visualization program ChimeraX[36,37] and docked the icosahedral asymmetric unit (IAU) models of Ad5 (PDB-ID: 6B1T)[49] and Ad6 (determined in our lab, unpublished) into the densities as rigid bodies. A composite model for Ad657 capsid was generated by combining an AlphaFold2[35] model for hexon with the rest of the Ad6 capsid proteins (e.g., PB, proteins IIIa, VI, VIII and IX), as the modified Ad657 vector used in these studies was built on the Ad6 backbone, by replacing the hexon HVRs of Ad6 with that of Ad57[32]. The Ad657 model was also similarly docked into the corresponding EM density. Subsequently, the docked models and the corresponding densities were moved into the model-building graphics program COOT[40,41]. Wherein the individual chains of each protein (hexon, PB, proteins IIIa, VI, VIII and IX) were adjusted as rigid bodies in the corresponding densities. The atomic models for the processed parts of FX (a.a. 41–488) and FII (a.a. 44–622) were generated using the AlphaFold2 program based on the UniProt a.a. sequences, P00742 and P00734, respectively. To account for the post-translational modifications of Glu residues, we manually replaced the 11 and 10 glutamic acid residues to Gla residues, in the N-terminal Gla domains of FX and FII models, respectively; and included the coordinating Ca^{2+} ions, by making use of the X-ray structure of the complex between FX binding protein from snake venom and the FX-Gla domain (PDB-ID: 1IOD)[50]. The models were then subjected to RS-refinement into the respective maps and followed by evaluating the models using various validation tools available in the program Phenix[38,39]. Because of the weak density, we did not include the models of the factors in the RS-refinement of virus-factor complexes. But we did include them in the RS-refinements involving localized reconstructions (see below). Of note, the densities of PBs were weak in most of the AdV maps and only the residues (27–105) of IIIa are ordered in all of the complex structures. The contacts between the Gla domains and the hexon subunits were calculated using the CONTACT program in CCP4[51] using a distance cutoff of 4.2 Å

https://doi.org/10.1038/s41467-024-54049-9

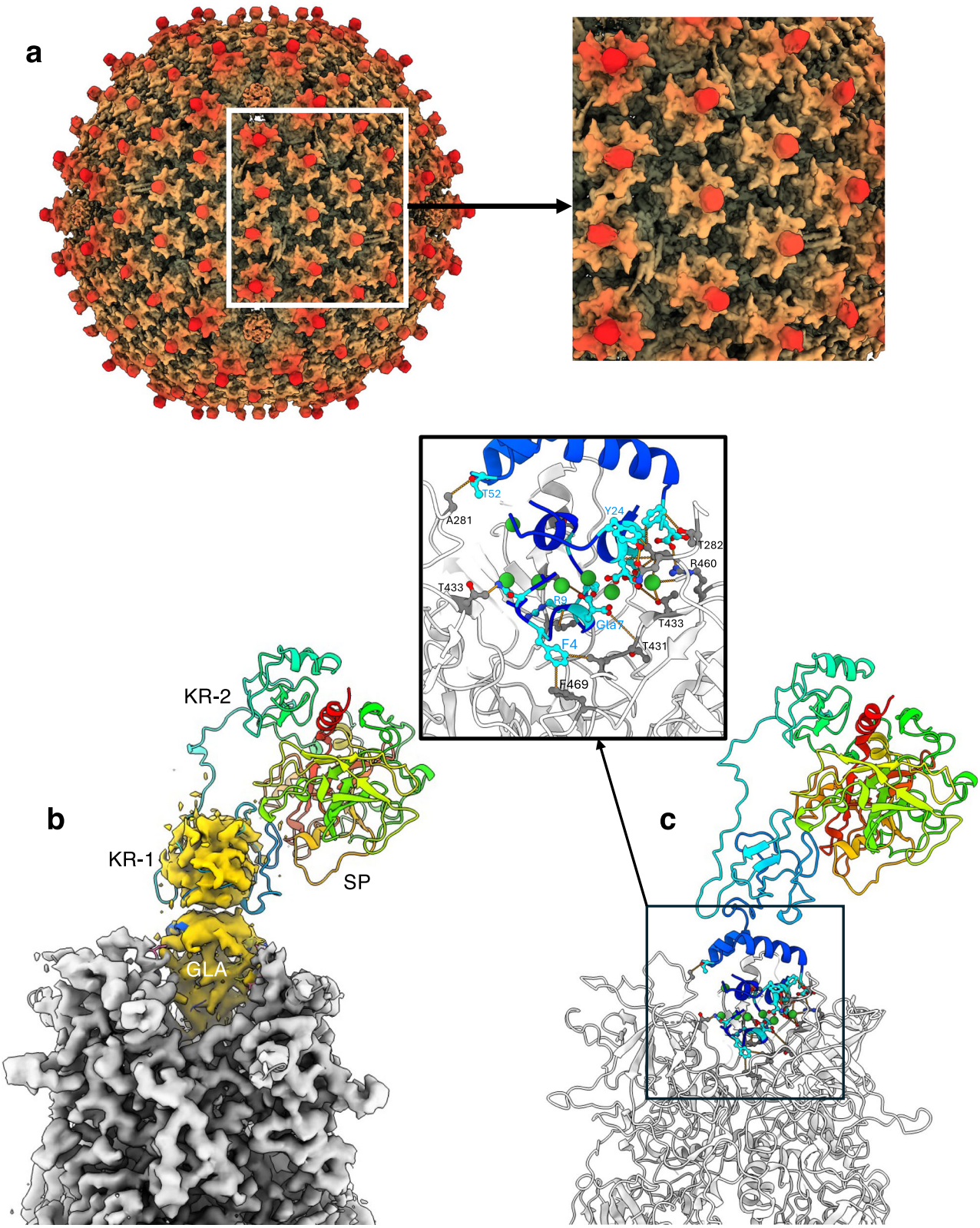

Fig. 4 | Cryo-EM reconstruction of Ad6-FII complex and hexon-FII interactions. **a** Icosahedral reconstruction of Ad6-FII complex at 3.7 Å resolution(contour level: 0.007). A radially color-coded representation with the bright red regions at the highest elevation corresponds to the bound FII molecules. Inset shows a zoomed-in view of the boxed area. **b** A localized reconstruction of hexon-FII complex at 3.86 Å (contour level: 0.01). A modified AlphaFold2 model of FII with Gla residues shown in rainbow color gradient, is docked into the corresponding density shown in yellow. While the densities corresponding to the Gla and KR1 domains can be seen, the densities corresponding to KR2, and SP domains are disordered. **c** Ad6:hexon-FII:Gla interactions. Inset shows a zoomed-in view of the boxed area of the FII-Gla binding site. Some of the interacting residues of the Gla domain (cyan) and hexon (gray), connected by the dotted lines, are shown in ball-and-stick representation and identified by blue and black labels, respectively. The Ca^{2+} ions are shown as green spheres. A complete list of interacting pairs of residues in Ad6:hexon-FII complex is given in Supplementary Table 3.

https://doi.org/10.1038/s41467-024-54049-9

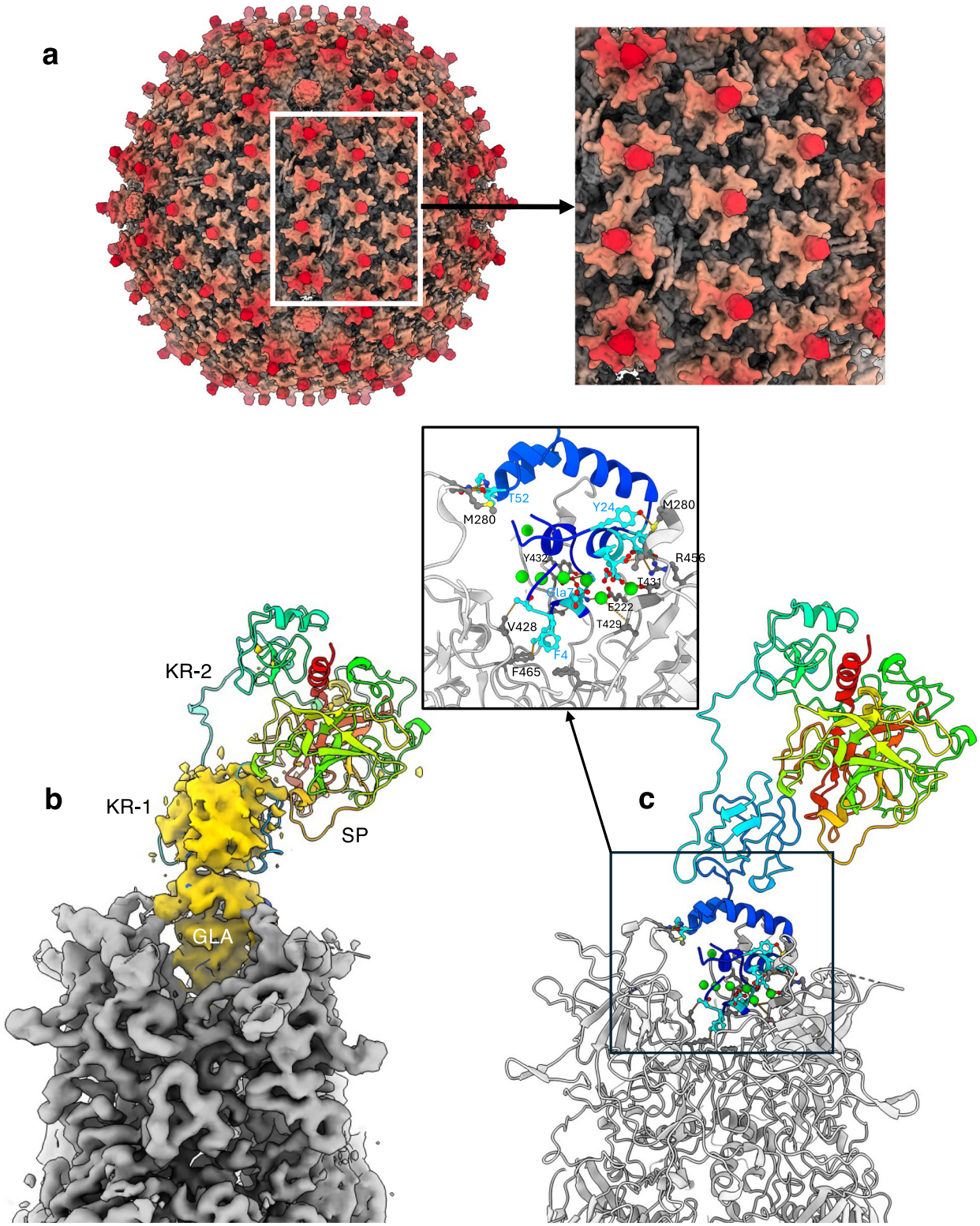

Fig. 5 | Cryo-EM reconstruction of Ad657-FII complex and hexon-FII interactions. a Icosahedral reconstruction of Ad657-FII complex at 4.2 Å resolution (contour level: 0.01). A radially color-coded representation with the bright red regions at the highest elevation corresponds to the bound FII molecules. Inset shows a zoomed-in view of the boxed area. **b** A localized reconstruction of hexon-FII complex at 4.1 Å (contour level: 0.004). A modified AlphaFold2 model of FII with Gla residues is docked into the corresponding density shown in yellow. As in the case of other Ad-FII complexes, only the densities corresponding to the Gla and KR1 domains can be seen, while the densities corresponding to KR2, and SP domains are disordered. **c** Ad657:hexon-FII:Gla interactions. Inset shows a zoomed-in view of the boxed area of the FII-Gla binding site. Some of the interacting residues of the Gla domain (cyan) and hexon (gray), connected by the dotted lines, are shown in ball-and-stick representation and identified by blue and black labels, respectively and the Ca^{2+} ions are shown as green spheres. A complete list of interacting pairs of residues in Ad657:hexon-FII complex are shown in Supplementary Table 3.

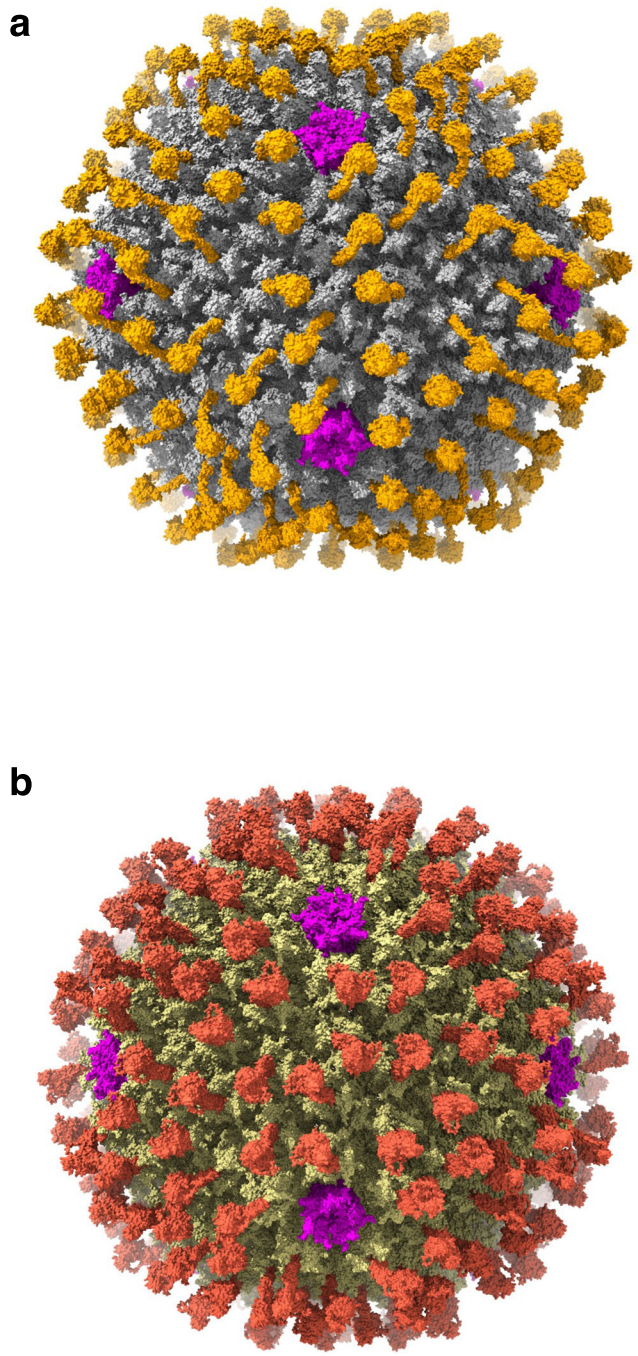

Fig. 6 | Illustrations of bound FX and FII molecules covering the surface of C-type AdV capsids. a Distribution of the bound FX molecules (orange) on the surface of Ad5 capsid (gray) generated based on the cryo-EM reconstruction of Ad5-FX complex (Supplementary Fig. 3). The locations of PBs are shown in magenta. The disordered fibers are not represented. **b** Distribution of the bound FII molecules (brick red) on the surface of Ad6 capsid (khaki) generated based on the cryo-EM reconstruction of Ad6-FII complex (Supplementary Fig. 9). The PBs are shown in magenta. The disordered fibers are not represented.

(Supplementary Tables 2 and 3). The surface Coulombic electrostatic potentials of the atomic models were calculated using ChimeraX[36,37].

Analysis of densities of coagulation factors FX and FII

To identify the location of FX and FII binding sites on the Ad5, Ad6 and Ad657 viruses, we subtracted model maps calculated using the respective models fitted into the reconstructed maps of the corresponding complexes in ChimeraX. The difference densities calculated at high resolution (~4.0 Å) based on various Ad-factor complex structures showed clear densities corresponding to the Gla domain of the coagulation factors in the hexon cavity formed by the hexon towers on the virus surface as previously observed (Supplementary Figs. 3–6, 8, 9, 11, 12, 16)[10,11]. Since these difference densities do not account for the complete FX/FII molecules, we calculated the difference densities at 10 Å resolution, which clearly showed blobby looking structures corresponding to EGF, KR1, KR2, and SP domains in some of the complexes (Supplementary Fig. 3), which otherwise are disordered at high resolution.

Localized reconstructions

The localized reconstructions of hexons in the respective AdV-Factor complexes were done according to the methods described by the authors of LocalRec program[33]. We used the implementation of localized reconstruction (LocalRec) in Scipion[34,52]. Briefly, after determining the canonical icosahedral reconstructions of the Ad-factor complexes as described above, we extracted the sub-regions around hexon-4 related by icosahedral symmetry after subtracting the core region (up to 300 Å radius) from the virus particle images (projections). The sub-particles were defined and extracted into a box size of 200x200x200 pixels (pixel size: 1.408) by aligning them to a standard orientation (Z-axis). These sub-particles were then subjected to 3D-classification into 6 classes employing C1 symmetry and without performing any alignments (–skip_align). The selected classes were then subjected to another round of 3D-classification with an atomic mask defined around the hexon-factor complex of interest. The selected classes were then subjected to 3D auto-refinement in C1 symmetry, with an atomic mask and relaxing the inherent C3 symmetry of the hexon-factor complexes (–relax_sym C3). The resulting map was subjected to post-processing, sharpened with a B-factor of -100 Å^2, and used for inspection and further analysis using the graphics programs, ChimeraX[36,37] and Coot[40,41] and RS-refinement using Phenix[38,39]. The details of the statistics of localized reconstructions are shown in Supplementary Table 4.

Reporting summary

Further information on research design is available in the Nature Portfolio Reporting Summary linked to this article.

Data availability

The cryo-EM maps of Ad5-FX, Ad5-FII, Ad6-FX, Ad6-FII, Ad657-FX and Ad657-FII have been deposited at EMDB with the accession codes EMD-51372, EMD-46615, EMD-46620, EMD-46654, EMD-46660 and EMD-46770, respectively. In addition, the localized reconstruction maps of Ad5:hexon-FX, Ad5:hexon-FII, Ad6:hexon-FX, Ad6:hexon-FII, Ad657:hexon-FX and Ad657:hexon-FII have been deposited at EMDB with the accession codes, EMD-45675, EMD-45726, EMD-45729, EMD-45737, EMD-45744 and EMD-45751, respectively. The corresponding PDB files based on the localized reconstructions have been deposited with the PDB-identifiers, 9CLI, 9CLN, 9CLS, 9CM2, 9CM9 and 9CMO, respectively. PDB codes of previously published structures used in this study are 6B1T and 1IOD. Source data are provided with this paper.

References

1. Campos, S. K. & Barry, M. A. Current advances and future challenges in Adenoviral vector biology and targeting. *Curr. Gene Ther.* **7**, 189–204 (2007).
2. Khare, R., Chen, C. Y., Weaver, E. A. & Barry, M. A. Advances and future challenges in adenoviral vector pharmacology and targeting. *Curr. Gene Ther.* **11**, 241–258 (2011).
3. Bailey, A. & Mautner, V. Phylogenetic relationships among adenovirus serotypes. *Virology* **205**, 438–452 (1994).
4. Arnberg, N. Adenovirus receptors: implications for tropism, treatment and targeting. *Rev. Med. Virol.* **19**, 165–178 (2009).

5. Weaver, E. A. et al. Characterization of species C human adenovirus serotype 6 (Ad6). *Virology* **412**, 19–27 (2011).
6. Crawford-Miksza, L. & Schnurr, D. P. Analysis of 15 adenovirus hexon proteins reveals the location and structure of seven hypervariable regions containing serotype-specific residues. *J. Virol.* **70**, 1836–1844 (1996).
7. Crawford-Miksza, L. K. & Schnurr, D. P. Adenovirus serotype evolution is driven by illegitimate recombination in the hypervariable regions of the hexon protein. *Virology* **224**, 357–367 (1996).
8. Kalyuzhniy, O. et al. Adenovirus serotype 5 hexon is critical for virus infection of hepatocytes in vivo. *Proc. Natl Acad. Sci. USA* **105**, 5483–5488 (2008).
9. Vigant, F. et al. Substitution of hexon hypervariable region 5 of adenovirus serotype 5 abrogates blood factor binding and limits gene transfer to liver. *Mol. Ther.* **16**, 1474–1480 (2008).
10. Waddington, S. N. et al. Adenovirus serotype 5 hexon mediates liver gene transfer. *Cell* **132**, 397–409 (2008).
11. Doronin, K. et al. Coagulation factor X activates innate immunity to human species C adenovirus. *Science* **338**, 795–798 (2012).
12. Manickan, E. et al. Rapid Kupffer cell death after intravenous injection of adenovirus vectors. *Mol. Ther.* **13**, 108–117 (2006).
13. Xu, Z., Tian, J., Smith, J. S. & Byrnes, A. P. Clearance of adenovirus by Kupffer cells is mediated by scavenger receptors, natural antibodies, and complement. *J. Virol.* **82**, 11705–11713 (2008).
14. Tian, J. et al. Adenovirus activates complement by distinctly different mechanisms in vitro and in vivo: indirect complement activation by virions in vivo. *J. Virol.* **83**, 5648–5658 (2009).
15. Khare, R., Hillestad, M. L., Xu, Z., Byrnes, A. P. & Barry, M. A. Circulating antibodies and macrophages as modulators of adenovirus pharmacology. *J. Virol.* **87**, 3678–3686 (2013).
16. Qiu, Q. et al. Impact of natural IgM concentration on gene therapy with adenovirus type 5 vectors. *J. Virol.* **89**, 3412–3416 (2015).
17. Tian, J. et al. Binding of adenovirus species C hexon to prothrombin and the influence of hexon on vector properties in vitro and in vivo. *PLoS Pathog.* **18**, e1010859 (2022).
18. Rodriguez, E. V. C. et al. Fatal vaccine-induced immune thrombotic thrombocytopenia (VITT) post Ad26.COV2.S: first documented case outside US. *Infection* **50**, 531–536 (2021).
19. Othman, M. et al. To clot or not to clot? Ad is the question-Insights on mechanisms related to vaccine-induced thrombotic thrombocytopenia. *J. Thromb. Haemost.* **19**, 2845–2856 (2021).
20. Greinacher, A. et al. Vaccine-induced immune thrombotic thrombocytopenia (VITT): Update on diagnosis and management considering different resources. *J. Thromb. Haemost.* **20**, 149–156 (2021).
21. Graf, T. et al. Immediate high-dose intravenous immunoglobulins followed by direct thrombin-inhibitor treatment is crucial for survival in Sars-Covid-19-adenoviral vector vaccine-induced immune thrombotic thrombocytopenia VITT with cerebral sinus venous and portal vein thrombosis. *J. Neurol.* **268**, 4483–4485 (2021).
22. Baker, A. T. et al. ChAdOx1 interacts with CAR and PF4 with implications for thrombosis with thrombocytopenia syndrome. *Sci. Adv.* **7**, eabl8213 (2021).
23. Alemany, R., Suzuki, K. & Curiel, D. T. Blood clearance rates of adenovirus type 5 in mice. *J. Gen. Virol.* **81**, 2605–2609 (2000).
24. Hofherr, S. E. & Barry, M. A. Near infrared fluorescence imaging to determine injection success in small animals. *Curr. Mol. Imaging* **4**, 53–56 (2015).
25. Xu, Z. et al. Coagulation factor X shields adenovirus type 5 from attack by natural antibodies and complement. *Nat. Med.* **19**, 452–457 (2013).
26. Parker, A. L. et al. Multiple vitamin K-dependent coagulation zymogens promote adenovirus-mediated gene delivery to hepatocytes. *Blood* **108**, 2554–2561 (2006).
27. Waddington, S. N. et al. Targeting of adenovirus serotype 5 (Ad5) and 5/47 pseudotyped vectors in vivo: fundamental involvement of coagulation factors and redundancy of CAR binding by Ad5. *J. Virol.* **81**, 9568–9571 (2007).
28. Khare, R. et al. Generation of a Kupffer cell-evading adenovirus for systemic and liver-directed gene transfer. *Mol. Ther.* **19**, 1254–1262 (2011).
29. Chesterman, C. N., McGready, J. R., Doyle, D. J. & Morgan, F. J. Plasma levels of platelet factor 4 measured by radioimmunoassay. *Br. J. Haematol.* **40**, 489–500 (1978).
30. Koldas, M. & Uras, F. Avidin-biotin ELISA for measurement of prothrombin in human plasma. *Thromb. Res* **102**, 221–227 (2001).
31. Irons, E. E. et al. Coagulation factor binding orientation and dimerization may influence infectivity of adenovirus-coagulation factor complexes. *J. Virol.* **87**, 9610–9619 (2013).
32. Nguyen, T. V. et al. Oncolytic adenovirus Ad657 for systemic virotherapy against prostate cancer. *Oncolytic Virother.* **7**, 43–51 (2018).
33. Ilca, S. L. et al. Localized reconstruction of subunits from electron cryomicroscopy images of macromolecular complexes. *Nat. Commun.* **6**, 8843 (2015).
34. Abrishami, V. et al. Localized reconstruction in Scipion expedites the analysis of symmetry mismatches in cryo-EM data. *Prog. Biophys. Mol. Biol.* **160**, 43–52 (2021).
35. Jumper, J. et al. Highly accurate protein structure prediction with AlphaFold. *Nature* **596**, 583–589 (2021).
36. Goddard, T. D. et al. UCSF ChimeraX: Meeting modern challenges in visualization and analysis. *Protein Sci.* **27**, 14–25 (2018).
37. Meng, E. C. et al. UCSF ChimeraX: Tools for structure building and analysis. *Protein Sci.* **32**, e4792 (2023).
38. Adams, P. D. et al. PHENIX: a comprehensive Python-based system for macromolecular structure solution. *Acta Crystallogr D. Biol. Crystallogr* **66**, 213–221 (2010).
39. Afonine, P. V. et al. Real-space refinement in PHENIX for cryo-EM and crystallography. *Acta Crystallogr. D Struct. Biol.* **74**, 531–544 (2018).
40. Emsley, P. & Cowtan, K. Coot: model-building tools for molecular graphics. *Acta Crystallogr. D Biol. Crystallogr.* **60**, 2126–2132 (2004).
41. Emsley, P., Lohkamp, B., Scott, W. G. & Cowtan, K. Features and development of Coot. *Acta Crystallogr. D. Biol. Crystallogr.* **66**, 486–501 (2010).
42. Alba, R. et al. Identification of coagulation factor (F)X binding sites on the adenovirus serotype 5 hexon: effect of mutagenesis on FX interactions and gene transfer. *Blood* **114**, 965–971 (2009).
43. Weaver, E. A. & Barry, M. A. Low seroprevalent species D adenovirus vectors as influenza vaccines. *PLoS ONE* **8**, e73313 (2013).
44. Shashkova, E. V., May, S. M. & Barry, M. A. Characterization of human adenovirus serotypes 5, 6, 11, and 35 as anticancer agents. *Virology* **394**, 311–320 (2009).
45. Matchett, W. E. et al. Divergent HIV-1-Directed Immune Responses Generated by Systemic and Mucosal Immunization with Replicating Single-Cycle Adenoviruses in Rhesus Macaques. *J Virol* **93**, e02016-18 (2019).
46. Zheng, S. Q. et al. MotionCor2: anisotropic correction of beam-induced motion for improved cryo-electron microscopy. *Nat. Methods* **14**, 331–332 (2017).
47. Mindell, J. A. & Grigorieff, N. Accurate determination of local defocus and specimen tilt in electron microscopy. *J. Struct. Biol.* **142**, 334–347 (2003).
48. Scheres, S. H. A Bayesian view on cryo-EM structure determination. *J. Mol. Biol.* **415**, 406–418 (2012).

49. Dai, X., Wu, L., Sun, R. & Zhou, Z. H. Atomic structures of minor proteins VI and VII in the human adenovirus. *J. Virol.* **91**, e00850-17(2017).
50. Mizuno, H., Fujimoto, Z., Atoda, H. & Morita, T. Crystal structure of an anticoagulant protein in complex with the Gla domain of factor X. *Proc. Natl Acad. Sci. USA* **98**, 7230–7234 (2001).
51. CCP4. The CCP4 suite: programs for protein crystallography. *Acta Crystallogr. D Biol. Crystallogr.* **50**, 760–763 (1994).
52. de la Rosa-Trevin, J. M. et al. Scipion: a software framework toward integration, reproducibility and validation in 3D electron microscopy. *J. Struct. Biol.* **195**, 93–99 (2016).

Acknowledgements

We would like to thank Dr. Juha Huiskonen, Helsinki Institute of Life Sciences, University of Helsinki for his generous advice on using Localized Reconstruction (LocalRec) program and Dr. Jeffrey McDonald, the director of HPC/IT at The Hormel Institute for installing Scipion, Relion, CryoSPARC and other EM software packages and help with running SLURM jobs on the HPC cluster. This work was supported by the NIH grant AI161367 to MAB and VSR and the startup funds to V.S.R. from the Hormel Foundation.

Author contributions

M.A.B. and V.S.R. conceptualized the study. M.E.B. expressed and purified various Ads. J.R.H. and F.G.M.A. carried out biochemical studies of PF4 binding to various Ads. H.E.M. and S.C.L. performed the biochemical experiments involving coagulation factors binding to various Ads and generated the corresponding Ad-factor complexes for the cryo-EM studies. J.B. and O.X.M. prepared the cryo-EM grids and collected the EM data. V.S.R. and O.X.M. processed the cryo-EM data, obtained 3D-reconstructions, generated 3D-atomic models and analyzed the structures. M.A.B. and V.S.R. supervised and funded the study. M.A.B. and V.S.R. wrote the manuscript with review and editing assistance from all authors.

Competing interests

The authors declare no competing interests.

Additional information

Supplementary information The online version contains supplementary material available at https://doi.org/10.1038/s41467-024-54049-9.

Correspondence and requests for materials should be addressed to Michael A. Barry or Vijay S. Reddy.

Peer review information *Nature Communications* thanks the anonymous reviewers for their contribution to the peer review of this work. A peer review file is available.